frontiers | Frontiers in Marine Science

TYPE Original Research
PUBLISHED 01 September 2025
DOI 10.3389/fmars.2025.1542584

OPEN ACCESS

EDITED BY
Naser A. Anjum,
Aligarh Muslim University, India

REVIEWED BY
Sumanta Kumar Mallik,
Directorate of Cold Water Fisheries Research (ICAR), India
Li Pu,
Sun Yat-sen University, China

*CORRESPONDENCE
Yongrui Pi
yrpi@outlook.com

RECEIVED 10 December 2024
ACCEPTED 28 July 2025
PUBLISHED 01 September 2025

CITATION
Jia W, Sun L, Li H, Lv T, Tang Y and Pi Y (2025) Adsorption of oxytetracycline hydrochloride by magnetic activated carbon: kinetics, mechanism and site energy distribution analysis.
Front. Mar. Sci. 12:1542584.
doi: 10.3389/fmars.2025.1542584

Adsorption of oxytetracycline hydrochloride by magnetic activated carbon: kinetics, mechanism and site energy distribution analysis

Wenpeng Jia[1], Lidong Sun[2], Huanjun Li[3], Tingjin Lv[2], Yongzheng Tang[1] and Yongrui Pi[1]*

[1]School of Ocean, Yantai University, Yantai, China, [2]Yantai Marine Econimic Research Institute, Yantai, China, [3]Shandong Marine Resource and Environment Research Institute, Yantai, China

The remove of oxytetracycline hydrochloride (OTC) antibiotics from water presents both significant challenges and importance. In this study, magnetic activated carbon (MAC) was synthesized from powdered activated carbon and ferric compounds using an alkaline co-precipitation process. Various characterizations techniques employed to assess the microscopic morphology, pore structure, and surface functionality of the adsorbents. The maximum equilibrium adsorption (q_m) of MAC for OTC at temperature of 20, 25, 30, 35, and 40°C were found to be 93, 112, 118, 108, and 117 mg/g, respectively, as determined by the Langmuir isotherm adsorption model. Thermodynamic and adsorption site energy analyses indicated that the adsorption process is a spontaneous endothermic reaction at elevated temperatures. During the OTC removal process, both chemisorption and physisorption mechanisms were observed, with adsorption site energies ranging from 4 to 16 kJ/mol, suggesting that chemical adsorption likely played a predominant role. The adsorbent material demonstrated excellent adsorption efficiency and a spontaneous nature, making it a promising candidate for the environmentally friendly treatment of antibiotic-contaminated wastewater.

KEYWORDS

magnetic activated carbon (MAC), oxytetracycline hydrochloride, adsorption kinetics, adsorption mechanism, site energy distribution analysis

1 Introduction

The worldwide production and consumption of antibiotics have significantly increased their emission into the natural environment from pharmaceutical industries, hospital wastes and veterinary drugs (Wang et al., 2019), which pose a potential threat to human health and natural ecological environment (Lu et al., 2020). Recent studies have detected antibiotic residues in both soil and water environments (Balzer et al., 2016; Wu et al., 2014),

which contribute to the emergence of antibiotic-resistant bacteria and genes, thereby destabilizing ecosystems (Wang et al., 2020). These resistant genes can persist in specific environments and spread throughout the ecosystem (Zhang et al., 2018), thus representing a new class of pollutants in contemporary society (Homem and Santos, 2011). Tetracyclines, macrolides, fluoroquinolones, and sulfonamides are among the most widely utilized antibiotics in aquatic environments worldwide (Li et al., 2018). Tetracyclines (TCs) are essential pharmaceutical antibiotics used to treat a variety of bacterial infections (Xu and Li, 2010) and are frequently incorporated into feed as medications for livestock diseases. Oxytetracycline hydrochloride (OTC) (Figure 1a), a representative tetracycline antibiotic, has been extensively used in animal feed and aquaculture due to its broad antimicrobial spectrum (Mihciokur and Oguz, 2016; Lian et al., 2013). The structure of OTC contains three dissociation sites (Figure 1b), leading to four predominant dissociation forms in aqueous solutions. In ambient water conditions, (pH 6-9), OTC typically exists in the dissociated states of $OTCH_2^0$, $OTCH^-$, OTC^{2-}. However, due to its low adsorption efficiency, a significant portion of OTC is not fully utilized and is discharged into the natural environment, resulting in ecological pollution (Badmus et al., 2018). Therefore, the removal of oxytetracycline antibiotics from water presents both a considerable challenge and significant importance.

The primary methods for removing antibiotics from wastewater include chemical oxidation (Badmus et al., 2018), degradation (Duan et al., 2017), plant uptake (Carter et al., 2014), membrane filtration (Nasrollahi et al., 2022), and adsorption (Zhao et al., 2016). Among them, physical adsorption stands out as a straightforward, cost-effective, and efficient technique for the removal of various antibiotics (Bednárek et al., 2024). Activated carbon is a commonly used adsorbent characterized by its large microporous volume, well-developed specific surface area, favorable pore size distribution, and high equilibrium adsorption (Hesas et al., 2013), particularly for antibiotics, dyes, and heavy metal ions. However, following its application in wastewater treatment, activated carbon is often disposed of alongside process sludge, which poses a risk of secondary pollution (Shao et al., 2012). In addition to their substantial adsorption capabilities, magnetic adsorbents present a promising solution to the urgent need for efficient extraction of adsorbents from aqueous solutions in antibiotic treatment. These magnetic adsorbents can be synthesized by incorporating heavy metal ions such as Co^{2+}, Ni^{2+}, and Fe^{3+} onto carbon-based or nanostructured materials through hydrothermal, coprecipitation, and microwave techniques (Li et al., 2020; Miao et al., 2021).

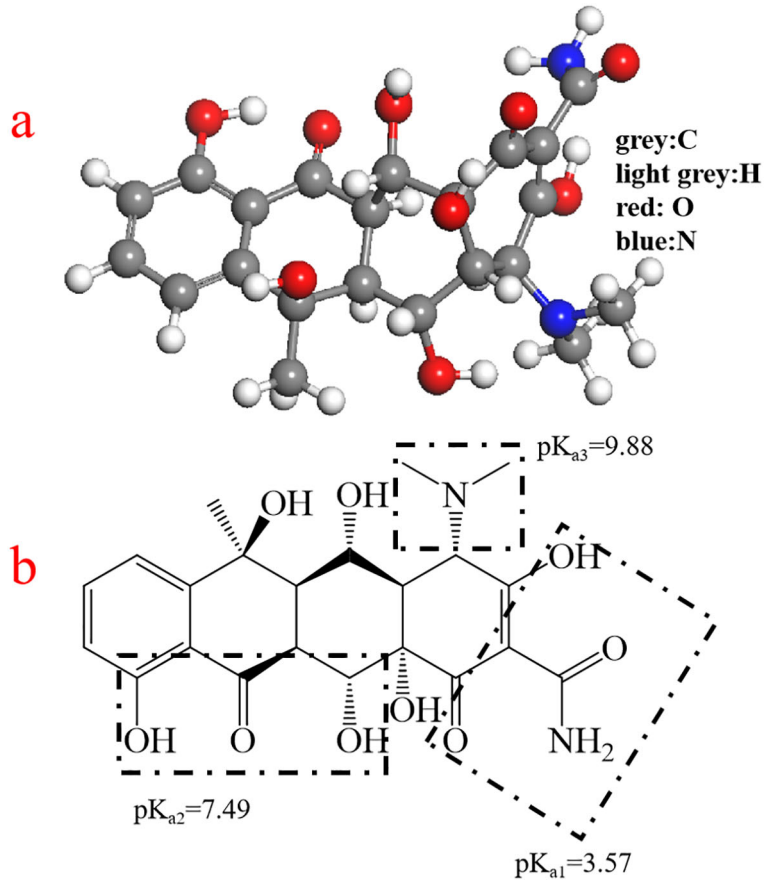

FIGURE 1
3D **(a)** and 2D **(b)** chemical structure of oxytetracycline (OTC).

Magnetic activated carbon (MAC) can be produced via hydrothermal methods (Yang et al., 2008), co-precipitation methods (Baghdadi et al., 2016) and other techniques utilizing activated carbon and iron compounds. MAC exhibits excellent equilibrium adsorption and benefits from the ease of magnetic separation (Li et al., 2020). Recently, more attention is being paid on the adsorption performance of MAC for OTC. Molecularly imprinted magnetic biochar (MBC@MIPs) just showed a maximum binding capacity of 67.9 mg/g for OTC (Jiao et al., 2024). The maximum adsorption ability of magnetic MMT-biochar composite was 58.9 mg/g for OTC (Liang et al., 2019). However, the adsorption ability is quite low, so it is necessary to further explore the adsorption performance of MAC for OTC more efficient and green.

In this study, MAC was synthesized using the alkaline co-precipitation method and utilized for the removal of OTC from water. To comprehensively investigate the interaction between the adsorbent and the adsorbate, this research aimed to: (1) analyze the morphology and structure of the magnetic activated carbon employing various characterization techniques; (2) evaluate the performance of the adsorbent for OTC removal through batch experiments, taking into account factors such as additive amount, OTC concentration, pH, temperature, and contact time; (3) analyze the distribution of adsorption site energy; and (4) explore the mechanisms underlying OTC adsorption.

2 Materials and methods

2.1 Chemical materials

Oxytetracycline hydrochloride was acquired from Shanghai Aladdin Biochemical Technology Co., Ltd. The chemicals $FeSO_4{\cdot}7H_2O$, $FeCl_3{\cdot}6H_2O$, H_2SO_4, HCl and NaOH were of analytical grade and sourced from various commercial suppliers without further purification.

2.2 Preparation of MAC

A total of 2.78 g of $FeSO_4{\cdot}7H_2O$, 5.40 g of $FeCl_3{\cdot}6H_2O$, and 2.89 g of powdered activated carbon were combined in 150 mL of deionized water and stirred vigorously at room temperature for 30 min. This mixture was then added drop wise to 60 mL of NaOH solution (2 mol/L) while maintaining a temperature of 70°C in a water bath, ensuring the solution pH≥12. After heating for 1 hour, the synthesized complex was washed 3-4 times with deionized water until the pH of the supernatant was neutral. The supernatant was discarded and the complex was dried in an oven at 60°C.

2.3 Characterizations of MAC

The morphology of the MAC before and after OTC adsorption was analyzed using field emission scanning electron microscopy (FESEM, JSM-7610F, Japan), transmission electron microscopy (TEM, JEOL-1400 Plus, Japan), X-ray diffraction (XRD, Shimadzu XRD-7000, Japan), fourier transform infrared spectroscopy (FT-IR, VERTEX70, Bruker, Germany), and X-ray photoelectron spectrometerscopy (XPS, ESCALAB 250Xi, USA). The microstructure was characterized by nitrogen adsorption at 77 K employing a fully automated chemisorption analyzer (BET, ASAP 2460, Micrometritics, USA). The magnetization of the MAC was measured using a vibrating sample magnetometer (VSM, LakeShore 7404, USA).

2.4 Adsorption experiments

To investigate the optimal adsorption conditions for OTC by MAC, we established a range of experimental several conditions, including solution concentration (10-100 mg/L), adsorbent mass (4-8 mg), pH (3-10), temperature (20-40°C) and adsorption time (0-240 min). These parameters were varied to determine the adsorption amount and removal rate of OTC.

To study the adsorption isothermal equilibrium, we set up experiments across three temperature gradients, with the initial OTC concentration ranging from 0 to 100 mg/L. All glass bottles used in the experiments were wrapped in tin foil to prevent photochemical reactions. Each experiment was conducted with agitation, and all trials were repeated three times for consistency.

The removal rate of OTC (adsorption percentage), as well as solid loading at time t and at equilibrium, were calculated using Equations 1–3):

$$R = \frac{C_0 - C_e}{C_0} \times 100 \tag{1}$$

$$q_t = \frac{C_0 - C_t}{\mathrm{m}} V \tag{2}$$

$$q_e = \frac{C_0 - C_e}{m} V \tag{3}$$

In these equations, R represents the removal efficiency of OTC; C_0 (mg/L), C_t (mg/L), and C_e (mg/L) denote the initial concentration, concentration at time t, and equilibrium concentration of OTC, respectively. Additionally, q_t (mg/g) and q_e (mg/g) represent the solid loading at time t and at equilibrium, respectively; while m (g) indicates the mass of the adsorbent and V (L) signifies the volume of the OTC solution.

2.5 Adsorption isotherms

Solutions of OTC at concentrations ranging from 10 mg/L to 100 mg/L were prepared and placed in 40 mL glass bottles with caps. Adsorption experiments for OTC were conducted at five different temperatures: 20, 25, 30, 35, and 40°C. Each experimental set-up consisted of three parallel groups.

The equilibrium adsorption of MAC for OTC was evaluated using the Langmuir (Langmuir, 1916), Freundlich (Freundlich, 1906),

and Temkin (Temkin and Pyzhev, 1940) isotherm equations (Pi et al., 2022; Carter et al., 1995) to further elucidate the influence of various forces on the adsorption process, following Equations 4–6.

$$\frac{C_e}{q_e} = \frac{C_e}{q_m} + \frac{1}{K_L q_m} \tag{4}$$

$$\ln q_e = \ln K_F + \frac{1}{n_F} \ln C_e \tag{5}$$

$$q_e = \left(\frac{RT}{b_T}\right) \ln (K_T C_e) \tag{6}$$

In this content, K_L (L/mg), K_F [(mg/g) (L/mg)$^{1/n}$] and K_T (L/mg) denote the adsorption coefficients for the Langmuir, Freundlich and Temkin models, respectively. The maximum equilibrium adsorption, q_m (mg/g), was calculated accordingly. The parameter $1/n_F$ represents the Freundlich model parameter, while b_T (L/mg) signifies the equilibrium constant for adsorption in the Temkin model (Yan et al., 2017).

2.6 Adsorption kinetics

In the kinetic experiments, of the adsorbate was used at a pH of 6 and a temperature of 30°C in 40 mL capped glass vials. The time intervals for the experiments were set at 10, 20, 30, 60, 120, 150, 180, 210, and 240 min, with three replicates for each time point.

The rate-controlled adsorption process was analyzed using the pseudo first-order (Lagergren, 1898), pseudo second-order (Ho and McKay, 1999) and Elovich model equations (Ritchie, 1977; Sun et al., 2022) as Equations 7–9.

$$\ln (q_e - q_t) = \ln q_e - k_1 t \tag{7}$$

$$\frac{t}{q_t} = \frac{1}{k_2 q_e^2} + \frac{t}{q_e} \tag{8}$$

$$q_t = \alpha + \beta \ln t \tag{9}$$

Here k_1 (h^{-1}) and k_2 (g/mg·h) represent the rate constants for the pseudo-first-order and pseudo-second-order kinetic models, respectively, while α and β are constants in the Elovich model.

To investigate the rate-limiting steps of the adsorption process, the intraparticle diffusion (IPD) model (Wang et al., 2010) and the liquid film diffusion (LFD) model (Hu et al., 2022; Foroutan et al., 2021) were employed Equations 10, 11.

$$-\ln (1 - F) = k_3 t \tag{10}$$

$$q_t = k_{IPD} t^{1/2} + c \tag{11}$$

Here k_3 (min^{-1}) denotes the liquid film diffusion rate constant, and F is calculated as q_t/q_e. The IPD diffusion rate constant, k_{IPD} [mg/(g·min$^{1/2}$)], along with the linear intercept, c (mg/g), provides insights into the boundary layer thickness.

2.7 Thermodynamic calculation

The thermodynamic parameters were calculated using the following equations, which help determine the nature of the adsorption process Equations 12–14.

$$\ln K_c = \frac{\Delta S}{R} - \frac{\Delta H}{RT} \tag{12}$$

$$\Delta G = -RT \ln K_c \tag{13}$$

$$K_c = \frac{q_e}{C_e} \tag{14}$$

In these equations, K_c (L/g) is the adsorption distribution coefficient, while ΔS (J/mol), ΔH (J/mol), and ΔG (J/mol·K) represent the changes in entropy, enthalpy, and Gibb's free energy, respectively. R (8.314 J/mol·K) is the gas constant, and T (K) is the temperature.

2.8 Site energy distribution analysis

The equilibrium adsorption of an adsorbent is linked to its adsorption site energy distribution (Carter et al., 1995). Utilizing the parameters from the Freundlich model, the following equation was derived:

$$E^* = E - E_s = RT \ln \left(\frac{C_s}{C_e}\right) \tag{15}$$

$$F(E^*) = \frac{q_m n b C_s^n}{RT} \bullet \frac{e^{-nE^*/RT}}{(1 + bC_s^n e^{-nE^*/RT})^2} \tag{16}$$

where E_s represents the adsorption energy, E^* denotes the difference in adsorption energy between the adsorbate and the solvent on the adsorbent surface, and $F(E^*)$ serves as an approximate potential energy distribution function. The maximum solubility of OTC (mg/L), denoted as C_s (mg/L), is essentially constant across different temperatures, with a value of 313 mg/L at room temperature (Kolar et al., 2014). Thus, the solubility of OTC in water is established as 313 mg/L.

The average site energy ($\mu(E^*)$) was evaluated using the following equation (Equation 17), which involves integral computation of the adsorption site energy distribution.

$$\mu(E^*) = \frac{\int_0^\infty E^* F(E^*) d(E^*)}{\int_0^\infty F(E^*) d(E^*)} \tag{17}$$

By integrating the above equation with Equations 15, 16, the average site energy can be determined as follows (Equation 18):

$$\mu(E^*) = \frac{RT}{n} \ln (1 + bC_s^n) \tag{18}$$

2.9 Statistical analysis

Each experiment has been carried out three times and the mean ± SD (standard deviation) has been considered for data analysis to confirm representative. The analysis was performed by using one-way ANOVA test. Values of $p < 0.05$ were considered statistically significant.

3 Results and discussion

3.1 Characterization of MAC

The TEM images presented in Figures 2a, b revealed that the inner composition consisted of activated carbon, with nano-Fe_3O_4 particles dispersed across the surface of MAC. Prior to adsorption, the peripheral regions exhibited distinct nanostructures, and the diameter of the adsorbent particles ranged from 0.5 to 1.0 µm. Post-adsorption (Figure 2b), the particle size appeared non-uniform. However, the nanostructures remained clearly visible. The SEM images (Figures 2e, i) illustrated the morphology of the adsorbed material both before and after the adsorption process, revealing a blocky structure in both cases. Initially, the surface was uneven, characterized by a pronounced pore structure. After adsorption, the pore structure became filled with OTC molecules, resulting in a relatively uniform and fuller surface on the adsorbent. Also, a denser interparticle lattice structure was created after OTC adsorption by zeolite/Fe_3O_4 particles (Baskan et al., 2022). Elemental mapping analysis (Figures 2f–h, j–l) indicated that the

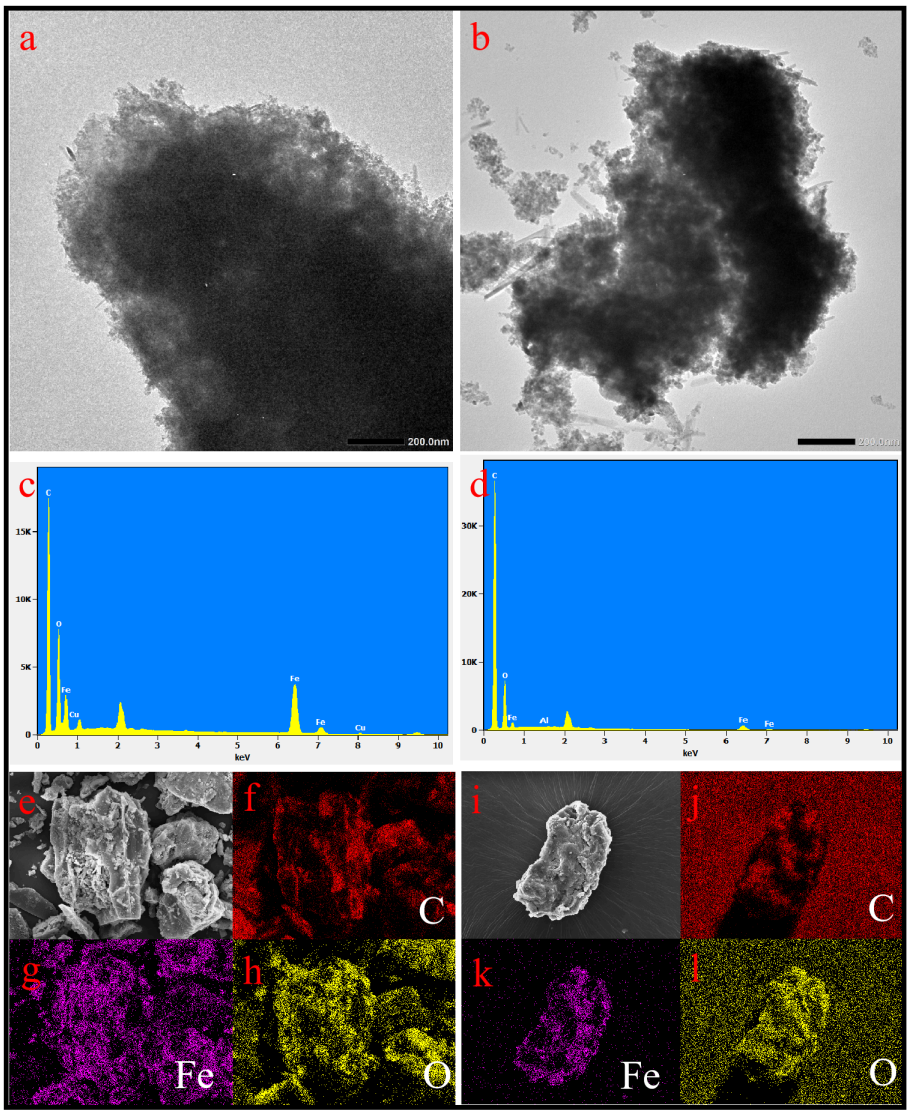

FIGURE 2
TEM images of MAC **(a)** pre-adsorption and **(b)** post-adsorption. EDX pattern of MAC **(c)** pre-adsorption and **(d)** post-adsorption. SEM images of MAC **(e)** pre-adsorption and **(i)** post-adsorption, and mapping images **(f–h)** pre-adsorption and **(j–l)** post-adsorption.

concentrations of C and O elements were higher following adsorption compared to before, attributed the presence of C and O in the OTC molecules. The EDS spectrum (Figures 2c, d) further confirmed the presence of C, O, and Fe within the structure. Notably, the intensity of the C signal significantly increased after OTC adsorption, while the intensity of the Fe signal exhibited a slight decrease.

Figure 3a illustrated the FTIR patterns of MAC before and after adsorption. The band observed near 580 cm^{-1} corresponded the Fe-O vibration of Fe_3O_4. Additionally, a minor absorption band at approximately 456 cm^{-1} indicated the presence of Fe_3O_4 (Zhang et al., 2023a). This observation confirmed that Fe_3O_4 could bond to activated carbon via the co-precipitation method, which aligned with the findings from the TEM images. The broad adsorption peak in the range of 3300-3400 cm^{-1} was typically associated with the O-H stretching vibrations (Duan et al., 2024). Following adsorption, the O-H peak shifted from 3367 cm^{-1} to 3379 cm^{-1}, indicating a red-shift attributable to OTC adsorption. The C=O stretching vibration, which originally peaked at 1577, shifted to 1569 cm^{-1} (Duan et al., 2024). The C-H stretching vibration detected at 1227 cm^{-1} and shifted to 1258 cm^{-1} post-adsorption. A new peak at 1337 cm^{-1} was identified as the C-O stretching vibration from OTC. The peak at

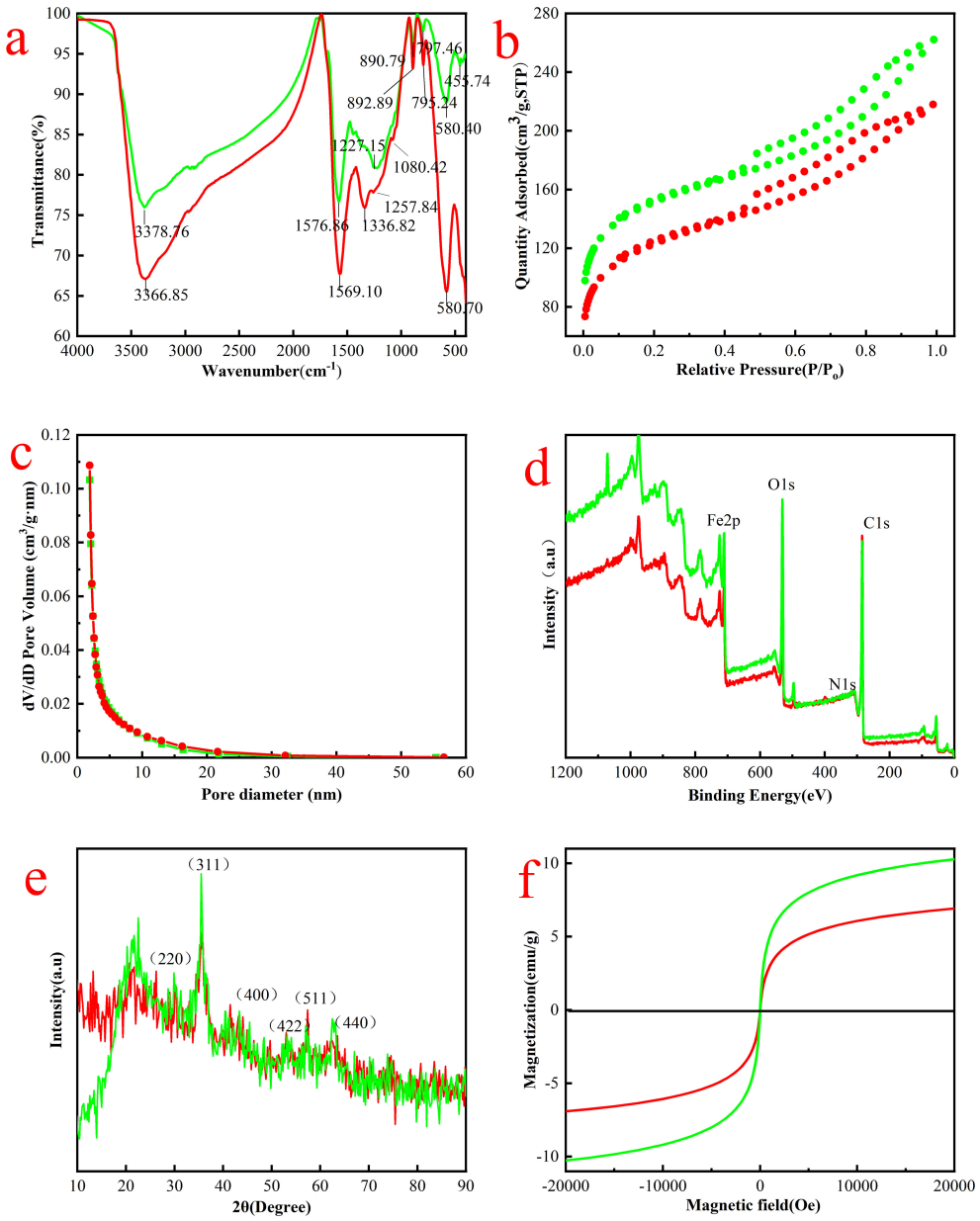

FIGURE 3
(a) FTIR images, **(b)** nitrogen adsorption and desorption isotherms and **(c)** Barrett-Joyner-Halendar (BJH) pore size distribution curves, **(d)** XPS spectra, **(e)** XRD patterns and **(f)** magnetic hysteresis loops for pre-adsorption (green) and post-adsorption(red).

1080 cm^{-1} was attributed to the in-plane bending vibration of the benzene ring C-H. Other peaks around 890 cm^{-1} and 800cm^{-1} were associated with out-of-plane bending vibrations of the meta-substituted benzene ring. Furthermore, several peaks observed after adsorption exhibited shifts compared to those before adsorption, indicating changes in the vibration energy required once OTC attached to the surface of MAC (Pi et al., 2022).

The specific surface area of the MAC was evaluated before and after adsorption using the adsorption-desorption model (Figure 3b). The composites exhibited favorable adsorption characteristics, particularly with increasing nitrogen concentration, across relative pressures of 0.1 to 1.0 (Saglam et al., 2024). Additionally, the average pore size distribution was determined through BJH isotherm analysis (Figure 3c). The findings indicated that the BET surface area was 555 m^2/g, while BJH adsorption and desorption average pore sizes of 4.8 nm and 4.4 nm, respectively, before adsorption. After adsorption, the BET surface area decreased to 446 m^2/g, with BJH adsorption and desorption average pore sizes of 4.4 nm and 4.0 nm. This data clearly demonstrated a reduction in both the BET surface area and BJH pore size of the MAC following adsorption. Similarly, both the surface area and the total pore volume of MagFePC-700 was decreased after adsorption of tetracycline (Gu et al., 2021).

XPS analysis was conducted to ascertain the elemental composition and valence states of the elements present in the samples. As illustrated in Figure 3d, the characteristic peaks at 285, 400, and 530 eV corresponded to C 1s, N 1s, and O 1s, respectively (Fatehi et al., 2017). The peaks at 710 and 725 eV for $Fe2p^{2/3}$ and $Fe2p^{1/2}$ respectively, indicated the coexistence of FeO and Fe_2O_3, contributing to the formation of the Fe_3O_4 molecule (Wu et al., 2023). Notably, the N characteristic peaks were less pronounced and less abundant, primarily associated with the OTC molecule, while the remaining the elements were present in

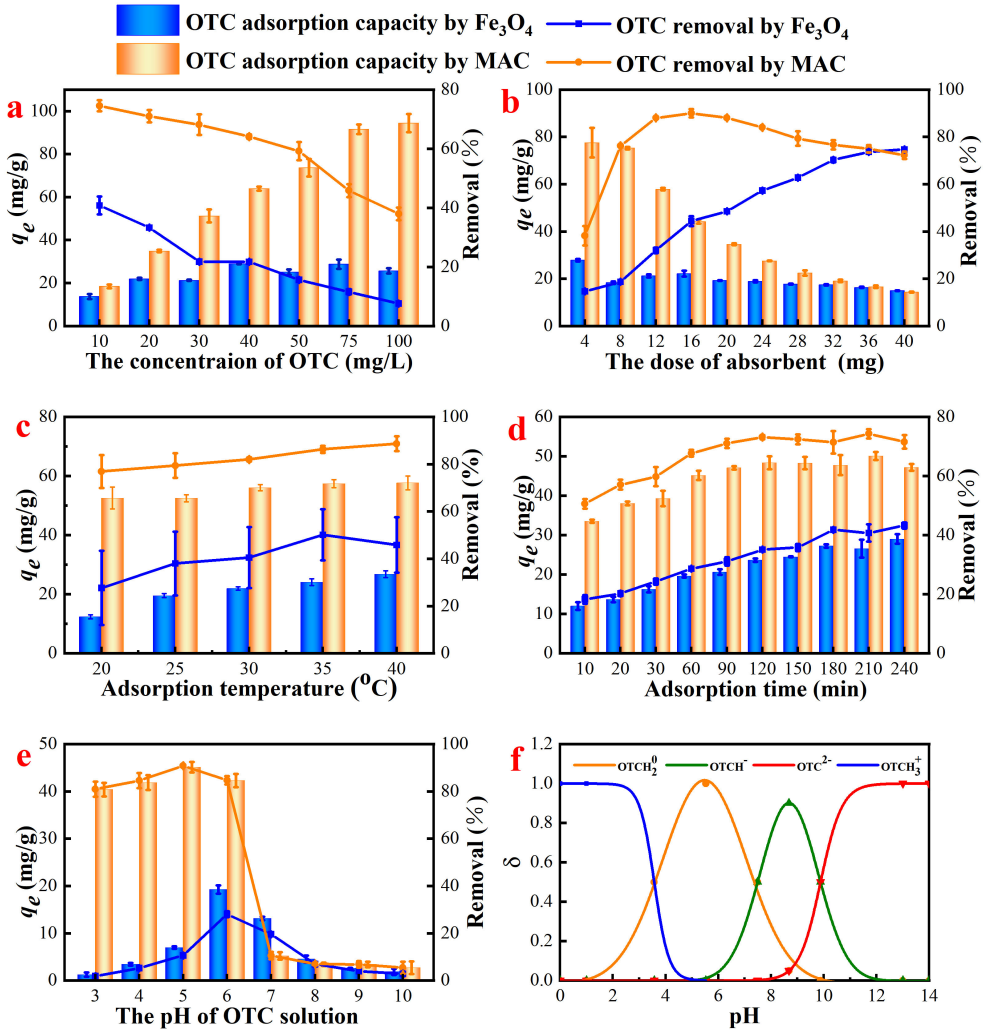

FIGURE 4
Adsorption properties of Fe_3O_4 and MAC on OTC under different adsorption conditions. **(a)**The initial concentrations of OTC, with the dosage of adsorbent 125 mg/L, pH = 7, T = 25 °C; **(b)** the concentration of adsorbent, with the OTC concentration of 50 mg/L, pH = 7, T = 25 °C; **(c)** the adsorption temperature, with the concentration of adsorbent 100 mg/L, the OTC concentration of 50 mg/L, pH = 7; **(d)** the adsorption time, with the concentration of adsorbent 100 mg/L, the OTC concentration of 50 mg/L, T = 30 °C; **(e)** the initial pH of OTC, with the concentration of adsorbent 100 mg/L, the OTC concentration of 50 mg/L, T = 30 °C, t = 2.0 h; and **(f)** the dissociation species distribution of OTC under different pH.

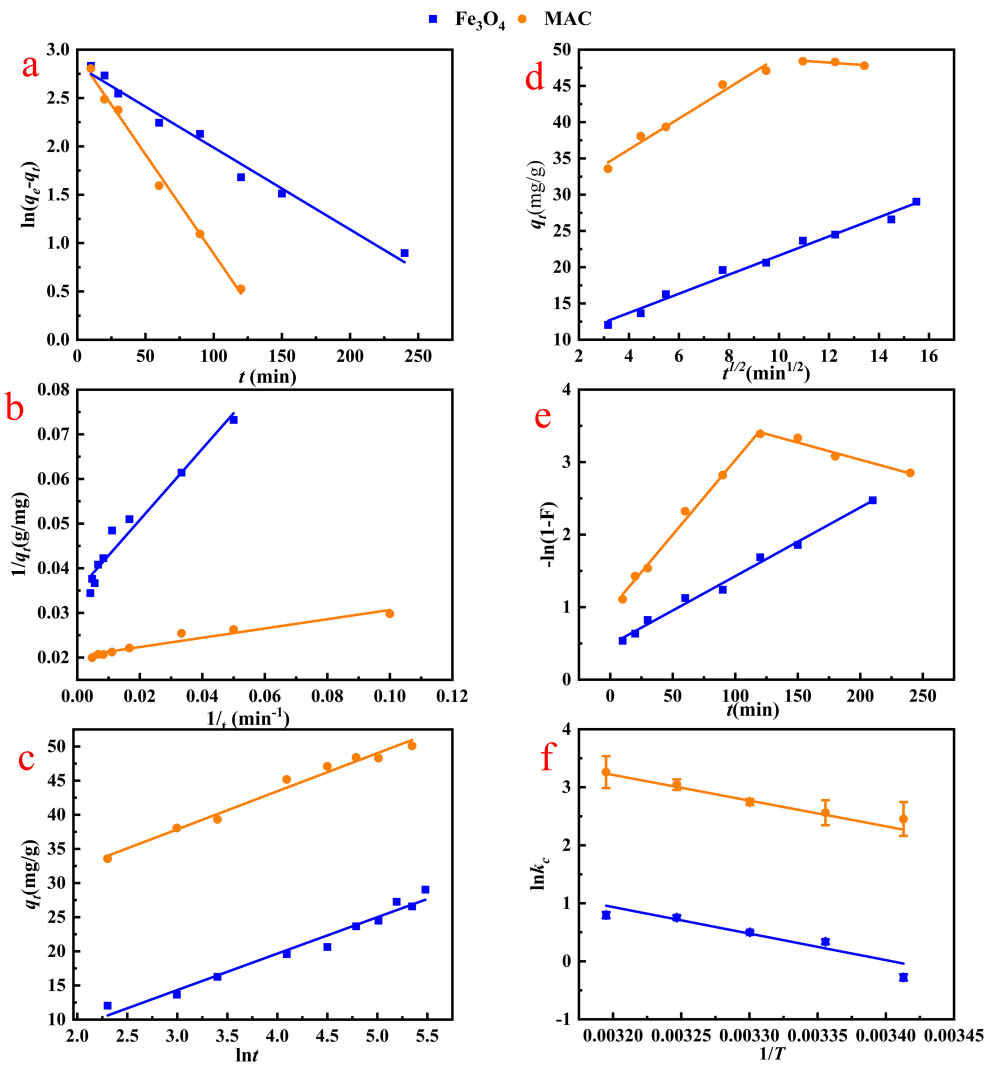

FIGURE 5
Kinetics of adsorption of OTC on Fe_3O_4 and MAC. **(a)** pseudo-first-order kinetics, **(b)** pseudo-second-order kinetics and **(c)** Elovich model. **(d)** The intraparticle diffusion model and **(e)** liquid film diffusion model of OTC adsorption by Fe_3O_4 and MAC. **(f)** Van,t Hoff model of OTC adsorption by Fe_3O_4 and MAC.

TABLE 1 Adsorption kinetic model on OTC using Fe_3O_4 and MAC.

Kinetic model	Model parameter	Fe3O4	MAC
	$q_{e,exp}$(mg/g)	29.0	50.1
Pseudo-first-order $\ln(q_e - q_t) = \ln q_e - k_1 t$	$q_{e,cal}$ (mg/g)	17.0	19.0
	k_1(1/min)	0.009	0.021
	R^2	0.980	0.992
Pseudo-second-order $\frac{t}{q_t} = \frac{1}{k_2 q_e^2} + \frac{t}{q_e}$	$q_{e,cal}$,(mg/g)	28.7	49.3
	k_2 (g/(mg·min))	0.002	0.005
	R^2	0.952	0.929
Elovich model $q_t = \alpha + \beta \ln t$	α	-1.68	21.1
	β	5.34	5.57
	R^2	0.965	0.978

TABLE 2 The IPD and LFD models on OTC using Fe_3O_4 and MAC.

The mass transfer process model	Model parameter	Fe_3O_4	MAC
IPD $q_t = k_{IPD} t^{1/2} + c$	k_{IPD1}	1.32	2.13
	C_1	8.43	27.7
	R_1^2	0.984	0.966
	k_{IPD2}	/	-0.25
	C_2	/	51.2
	R_2^2	/	0.693
LFD $-\ln(1 - F) = k_3 t$	k_3^1	0.010	0.021
	R_1^2	0.990	0.992
	k_3^2	/	-0.005
	R_2^2	/	0.944

TABLE 3 Adsorption equilibrium isotherm models on OTC using Fe_3O_4 and MAC.

Isothermal adsorption model	Model parameter	Adsorption temperature of OTC									
		20°C		25°C		30°C		35°C		40°C	
		MAC	Fe_3O_4	MAC	Fe_3O_4	MAC	Fe_3O_4	MAC	Fe_3O_4	MAC	Fe_3O_4
Langmuir isothermal adsorption $\frac{C_e}{q_e}=\frac{C_e}{q_m}+\frac{1}{K_L q_m}$	q_m,(mg/g)	93	45	112	30	118.5	29	108	33	117	47
	K_L (L/mg)	0.175	0.029	0.126	0.152	0.128	0.200	0.226	0.942	0.340	0.081
	R^2	0.953	0.941	0.966	0.622	0.971	0.440	0.924	0.435	0.988	0.943
Freundlich isothermal adsorption $\ln q_e=\ln K_F+\frac{1}{n_F}\ln C_e$	K_F ((mg/g)(L/mg)$^{1/n}$)	36.3	2.9	35.8	7.9	37.9	17.4	40.7	22.9	51.2	13.8
	n_F	4.84	1.79	3.96	3.12	3.94	9.44	4.30	11.2	4.13	4.00
	R^2	0.985	0.849	0.789	0.749	0.741	0.532	0.830	0.305	0.959	0.957
Temkin isothermal adsorption $q_e=(\frac{RT}{b_T})\ln(K_T C_e)$	b_T (J/mol)	208.3	228.3	118.2	294.4	113.1	750.2	163.5	574.8	183.3	273.1
	K_T (L/mg)	20.7	0.26	2.03	0.65	2.07	53.2	11.5	64.8	51.0	1.01
	R^2	0.955	0.758	0.870	0.731	0.842	0.369	0.783	0.759	0.903	0.930

substantial quantities within the MAC. The percentage of C increased from 61.7% to 69.9% due to OTC adsorption, whereas the percentage of O and Fe exhibited a slight decrease following adsorption.

In the XRD patterns, the characteristic crystal planes of Fe_3O_4, namely (220), (311), (400), (422), (511), and (440), were observed at 30.2°, 35.6°, 43.3°, 53.4°, 57.1°, and 62.5°, respectively (Zhou et al., 2020). Notably, these planes remain at the same positions in the XRD spectra of Fe_3O_4 following the compounding process (Figure 3e), indicating that the crystal structure of Fe_3O_4 was preserved during the material composite process. Additionally, two weak diffraction peaks corresponding to activated carbon were observed at 25.5° (576) and 44.5° (488), which confirmed the successful composite formation of Fe_3O_4 with activated carbon (Aravind et al., 2022).

TABLE 4 Comparison of the adsorption capacities of different magnetic adsorbents for the removal of OTC at ambient temperatures (25°C).

Adsorbent	$Q_{m,exp}$ (mg/g)	Reference
MF-CMS	98.7	Zhang et al., 2023a
zeolite/Fe_3O_4	18.9	Baskan et al., 2022
FeNiZn-LBC	272	Lin et al., 2022
ZnFe-LDH/MBC	140	Li et al., 2022
MIL-53(Al)@CBS	72.4	Cevallos-Mendoza et al., 2024
Carbon-Fe_3C/lignin	161	Liu et al., 2023
Carbon-MIL-101-NH_2	93.6	
MIL-101-NH_2 (Fe)	193.5	
NH-ZVI@$BC_{1.5/1/5}$	88	He et al., 2023
NHZVI@$BC_{5/1/5}$	177	
MWCNTs-$CuNiFe_2O_4$	388	Ma et al., 2023
1S-MLDH1:1	97	Smata and Yoshimura, 2022
1S-MLDH1:2	103	
1S-MLDH1:3	116	
1S-MLDH1:4	104	
2S-MLDH1:2	70	
2S-MLDH1:3	79	
Fe_3O_4@MAC	114.6	This work

The magnetic behavior of the MAC at room temperature, along with the respective magnetization hysteresis loops, were evaluated using vibrating sample magnetometry (VSM), as illustrated in Figure 3f. The coercivity and remanent magnetization of the MAC, both before and after adsorption, were found to be nearly zero. This suggested that the magnetism of the material dissipated immediately upon the removal of the applied magnetic field, indicating that the adsorbent exhibited superparamagnetic without hysteresis (Zhou et al., 2019). Furthermore, the magnetization intensity after adsorption (6.9 emu/g) was significantly lower than that prior to adsorption (10.3 emu/g). This observation aligned with the diminished peak of Fe in the XPS results after adsorption, suggesting that the material, per unit mass, contained less elemental Fe post-adsorption, while remaining sufficiently stable for magnetic separation.

3.2 Adsorption properties of OTC by MAC

3.2.1 Effect of initial concentration of OTC

The initial concentration of antibiotics significantly influenced the adsorption performance of the MAC and served as a benchmark for evaluating the suitability of the adsorbent for treating real wastewater containing varying concentrations of OTC. Figure 4a illustrated the effect of MAC on the equilibrium adsorption and removal efficiency of OTC at different initial concentrations. The maximum equilibrium adsorption of Fe_3O_4 was observed to be 29

TABLE 5 Thermodynamic model of adsorption.

Adsorbent	ΔH^{θ}(kJ/mol)	ΔS^{θ}(J/(mol·K))	ΔG^{θ}(kJ/mol)				
			293.15(K)	298.15(K)	303.15(K)	308.15(K)	313.15(K)
Fe_3O_4	38.0	129.4	0.68	-0.84	-1.26	-1.93	-2.07
MAC	36.8	144.5	-5.98	-6.35	-6.92	-7.80	-8.49

mg/g at an initial concentration of 40 mg/L. As the initial concentration of OTC increased, the equilibrium adsorption of MAC rose correspondingly, reaching a peak of 94.5 mg/g. This enhancement could be attributed to the reduction in volume transfer resistance between the adsorbent and solute molecules as the concentration of the solution increased, thereby facilitating greater adsorption. However, it was important to note that despite the increase in equilibrium adsorption, the percentage of solute adsorbed decreased with rising solution concentration, leading to a reduction in the overall removal rate.

3.2.2 Effect of adsorbent dosage

Figure 4b illustrated the impact of adsorbent quantity on equilibrium adsorption and removal efficiency. As the mass of MAC increased from 4 mg to 40 mg, corresponding to a dosage range of 100-1000 mg/L, the equilibrium adsorption exhibited a decrease, while the removal rate initially increased before subsequently decreasing. The rise in adsorbent dosage resulted in an expanded surface area of MAC, an increased number of adsorption sites (Altaf et al., 2021), and a higher total adsorption volume, thereby enhancing the removal rate. However, the specific surface area diminished due to the aggregation of the adsorbent (Fang et al., 2021a), leading to a reduction in equilibrium adsorption despite the overall increase in total adsorption. Although the increase in Fe_3O_4 dosage did not significantly affect the decrease in equilibrium adsorption, at lower dosage, both the equilibrium adsorption and removal rate were markedly inferior compared to MAC.

3.2.3 Effect of adsorption temperature

The effect of temperature is critical to the equilibrium adsorption of the adsorbent, providing valuable insights into the adsorption mechanism. As the temperature increased, the equilibrium adsorption of OTC also slightly rose (Figure 4c), which aligned with the observation that most adsorption processes were endothermic reactions (Zhang et al., 2023a). The heightened molecular motion at elevated temperatures facilitated the movement of OTC molecules to the surface of MAC, necessitating additional energy input. Higher temperatures increase the kinetic energy of molecules and reduce fluid viscosity, leading to faster diffusion to the adsorbent surface. Additionally, higher temperatures provide more molecules with sufficient energy to overcome an activation energy barrier, increasing the adsorption.

3.2.4 Effect of adsorption time

The influence of time on the adsorption process of MAC with OTC was illustrated in Figure 4d. The initial ten minutes exhibited rapid adsorption, followed by a gradual decrease in the rate of adsorption, with equilibrium being approached after 120 min. In contrast, the control group, Fe_3O_4, demonstrated a slower adsorption rate, reaching equilibrium after 180 min with both the

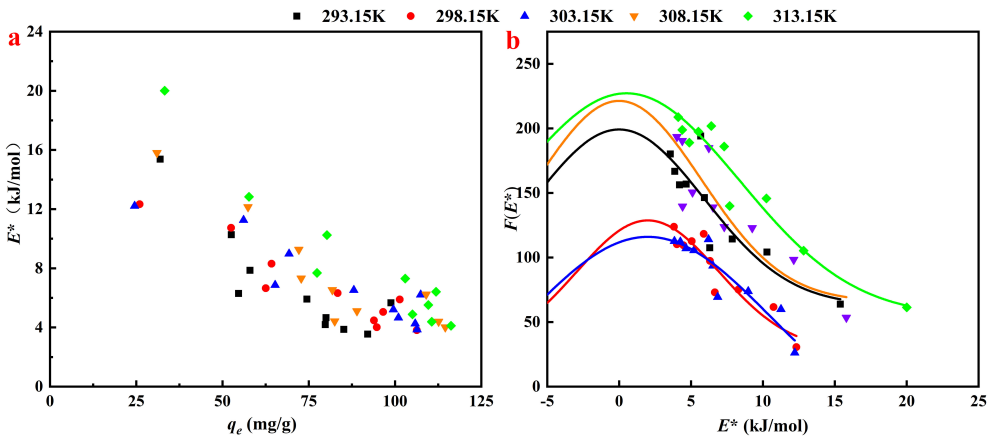

FIGURE 6
(a) Site energy versus equilibrium OTC equilibrium adsorption by MAC. **(b)** Site energy distribution of OTC adsorption by MAC at various temperatures.

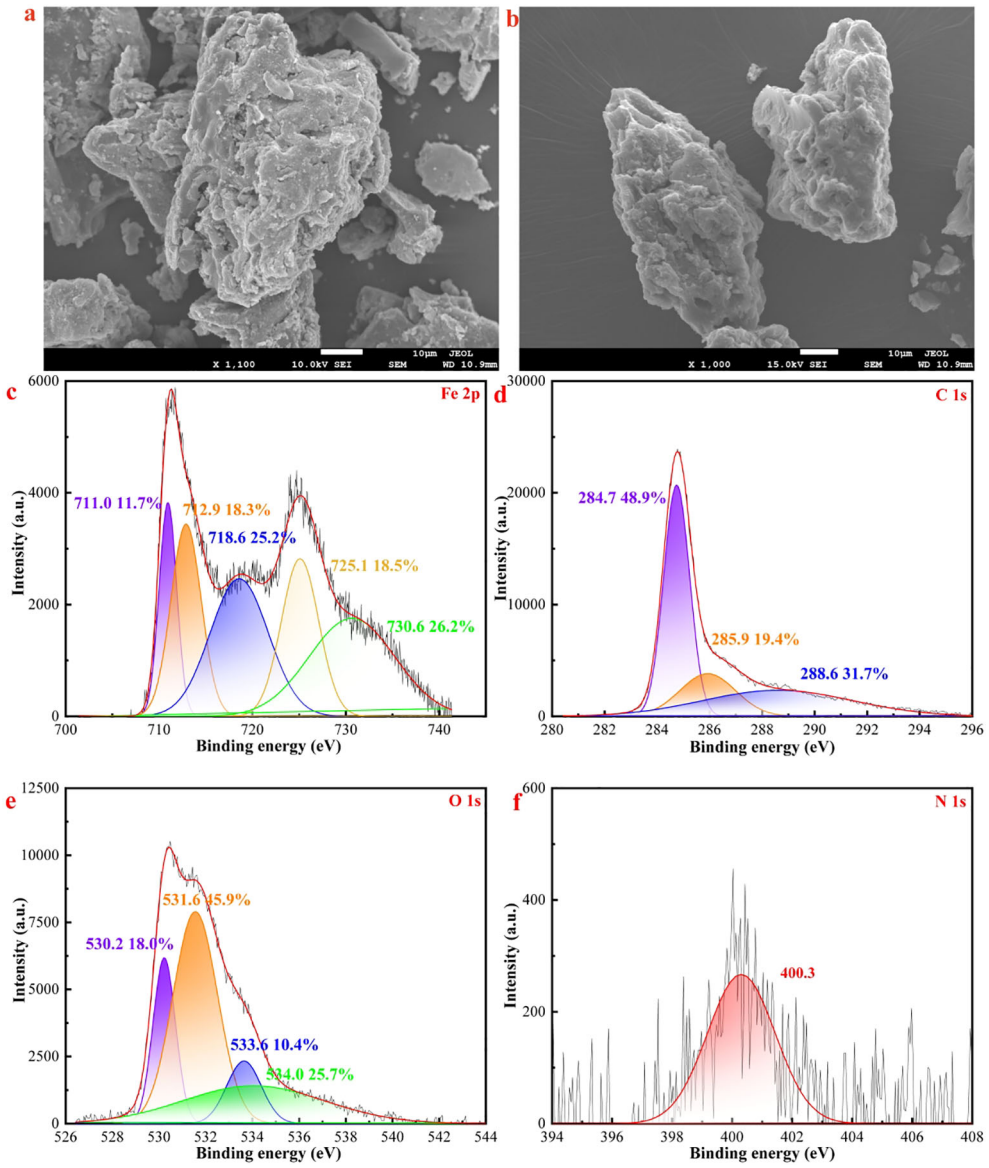

FIGURE 7
SEM images of MAC **(a)** pre-adsorption and **(b)** post-adsorption, high solution spectrum of **(c)** Fe 2p **(d)** C 1s, **(e)** O 1s, and **(f)** N 1s of the MAC after adsorption of OTC.

maximum equilibrium adsorption and removal rate being significantly lower than those of the experimental group. Once adsorption equilibrium was achieved, the system reached a dynamic state where the rates of adsorption and desorption were approximately equal.

3.2.5 Effect of pH

The influence of pH on adsorption is significant, primarily because it alters the surface charge of the adsorbent and affects the ionization of solution molecules (Fang et al., 2021b). The ionization of OTC is particularly sensitive to pH due to its three ionizable functional groups, which have pK_a values of 3.57, 7.49, and 9.44, respectively (Figure 4f) (Andrade et al., 2020). When the pH was from 4 to 7, OTC mainly existed in the form of zwitterions. The electrostatic repulsion between MAC and OTC was reduced, causing that the removal efficiency of MAC on OTC was improved. Also, the π–π electron donor-acceptor (EDA) interaction between $OTC^{\pm}$ and MAC would be strengthened (Zeng et al., 2024). As illustrated in Figure 4e, MAC exhibited strong adsorption performance. The anionic species of OTC^{-} and OTC^{2-} began to form at pH 5.6 and 7.46, while the MAC surface also became more negatively charged. Conversely, OTC carried negative charge when pH>8, resulting in the electrostatic repulsion between the two, which diminished the equilibrium adsorption (Lye

et al., 2017; Wu et al., 2023). Similar result was found that the q_e of OTC by nanosized activated carbon in aquatic environments (Zeng et al., 2024). In contrast, Fe_3O_4 demonstrated superior adsorption performance under neutral conditions. However, both the equilibrium adsorption and removal rate were markedly lower than those of MAC.

3.3 Adsorption kinetics

The removal rate of OTC by MAC can be partially predicted through adsorption kinetics, which also offers insights into the adsorption mechanism of OTC on MAC. The fitting of the three adsorption kinetic models is shown in Figure 5 and Table 1. The experimental data aligned more closely with the aforementioned models, exhibiting R^2 values greater than 0.92. The pseudo-first-order kinetic model is more suitable to fit the adsorption data. Most experts believed that the pseudo-second-order kinetic model could be divided into two stages. Initially, OTC molecules were adsorbed onto the microporous surface of MAC, forming a monolayer. The rate of the adsorption was regulated by the surface reaction process rather than the mass transfer process (Yan et al., 2020). As the physical adsorption of the monolayer approached saturation, OTC adsorption was influenced by chemical interactions, such as valence forces and electron exchange. Additionally, the mass transfer resistance between the OTC solution and MAC was mitigated by the presence of conjugated π-π interactions or -OH bonds (Song et al., 2021). The results from the pseudo-second-order model calculations indicated that the estimated maximum adsorption capacities of MAC and Fe_3O_4 for OTC were 49.3 mg/g and 27.7 mg/g, respectively. These values were close agreement with to the experimental adsorption capacities of 50.1 mg/g and 29.0 mg/g (Table 1). Furthermore, the adsorption rate constant $k_2$was significantly lower than 1, suggesting that the adsorption process was rapid.

Based on the mass transfer process model, there was just one step for OTC adsorption by Fe_3O_4, while for MAC, the adsorption of OTC could be identified into two kinetic phases (Figures 5d, e and Table 2). The first stage was characterized by a rapid surface adsorption process with a higher k_{IPD1}(k_{IPD1} = 2.13, k_3^1 = 0.021), which was controlled by the rate constants. During this stage, OTC is quickly adsorbed onto the MAC surface. The second stage represented a typical adsorption saturation process (k_{IPD2} = -0.25, k_3^2 = -0.005). As surface sites became occupied in the first stage, OTC began to interact with the functional groups within the pores of the material, leading to establishment of a dynamic equilibrium (Song et al., 2021; Xiang et al., 2022). The observation that none of the linear passed through the origin's coordinates in Figures 5d, e indicated the presence of rate-limiting steps beyond intraparticle diffusion. Consequently, both intraparticle diffusion and liquid film diffusion concurrently influence the rate-limiting step of the adsorption process. The R^2 values for both IPD and LFD models did not exhibit significant difference (Table 2), further suggesting that the initial two stages collectively impact the mass transfer process of adsorption.

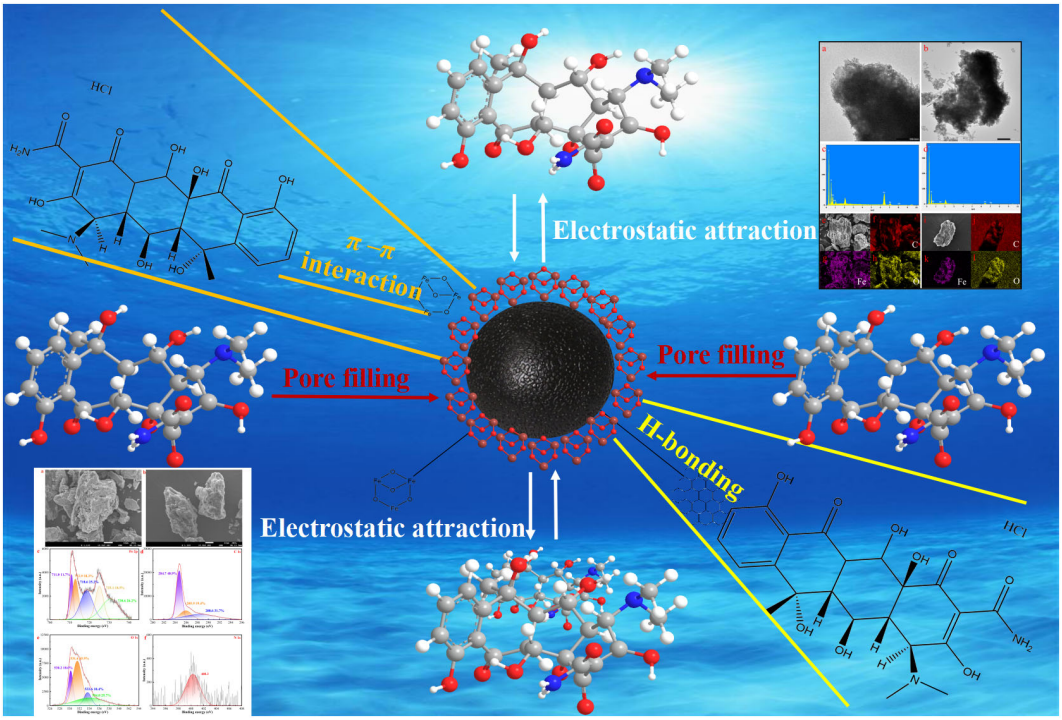

FIGURE 8
Schematic diagram of the adsorption mechanism of OTC by MAC.

3.4 Adsorption isotherm and thermodynamics analysis

Table 3 presented the results of three adsorption isotherm models applied to fit the adsorption of OTC onto MAC and Fe_3O_4. Notably, the R^2 values for the Langmuir model were significantly higher than those of the Freundlich and Temkin models, indicating a better fit. The Langmuir model suggested that the adsorption process was primarily governed by monomolecular layer adsorption. Conversely, the Freundlich model, n_F>1 (1~10), indicated that substantial adsorbent/adsorbate interactions occurred, highlighting MAC as a favorable candidate for OTC adsorption (Lv et al., 2020; Zhang et al., 2023b). The maximum adsorption capacities of MAC for OTC, as evaluated by the Langmuir adsorption model at temperatures of 20, 25, 30, 35, and 40°C, were 93, 112, 118.5, 108 and 117 mg/g, respectively.

The equilibrium adsorption for OTC of MAC of MAC for OTC, compared to other reported materials, was presented in Table 4. As indicated in Table 4, the OTC adsorption performance of MAC significantly exceeds that of Fe_3O_4-derived carbon materials (Zhang et al., 2021) and surpasses several biochar-derived porous carbon materials. Therefore, MAC emerged as a potentially effective adsorbent for the removal of OTC contaminants.

Research into adsorption thermodynamics aimed to enhance our understanding of the energy changes that occurred during the adsorption process and to provide theoretical guidance for the synthesis, performance improvement, and application of adsorption materials. Consequently, Equations 12–14 were employed to perform the thermodynamic analysis. The relevant parameters and thermodynamic graphs were presented in Table 5 and Figure 5f. The ΔG values for all adsorbents were consistently negative and decreased with increasing temperature, which further indicated that the adsorption of OTC by both MAC and Fe_3O_4 was a spontaneous process. This spontaneity was observed as the temperature rose from 293.15 K to 313.15 K. Additionally, the positive ΔH values confirmed that the adsorption of OTC by MAC and Fe_3O_4 was an endothermic process, suggesting that higher temperatures facilitated adsorption. Furthermore, the positive ΔS values indicated that OTC molecules were adsorbed randomly on the surfaces of MAC and Fe_3O_4.

3.5 Adsorption site energy analysis

As illustrated in Figure 6a, the adsorption potential energy E^* at various temperatures was determined using Equation 15. Notably, as the equilibrium adsorption increased, the value of E^* decreased dramatically. This observation suggested that the OTC molecules initially occupied high-energy adsorption sites during the early stages of the adsorption process. As the concentration of OTC molecules increased, they were subsequently forced to occupy lower-energy adsorption sites. Furthermore, the value of E^* increased markedly with rising temperature, suggesting that temperature was a primary factor influencing the energy of the adsorption sites, and that elevated temperatures enhanced the adsorption process (Cheng et al., 2023). This finding was consistent with the results derived from thermodynamic analysis.

A Gaussian distribution was fitted to E^* versus $F(E^*)$, revealing a single-peak distribution of the energy distribution. The approximate site energy distribution, $F(E^*)$, was derived based on Equation 16 and the parameters from the Freundlich model, as depicted in Figure 6b. The adsorption predominantly occurred at sites with energies ranging from 4.0 kJ/mol to 16.0 kJ/mol, suggesting that the adsorption process was predominantly physico-chemical in nature (Tang et al., 2023). The main cause of the energy distribution is the hybrid nature of the material structure. The surface of iron oxides has high-energy sites such as ≡Fe-OH, and the carbon matrix provides low-energy van der Waals interaction sites. For OTC adsorption, the low-energy sites have a significant contribution to the adsorption of high-concentration of OTC.

Based on the analysis of kinetics and site energy data, MAC demonstrates high suitability for continuous/large-scale wastewater treatment, with distinct advantages in separation efficiency, kinetics, and operational stability. MAC follows pseudo-first-order kinetic model (Table 1; Figure 5), indicating the adsorption process with fast initial adsorption rates. MAC achieves more than 95% recovery within 1 min using external magnets, eliminating energy-intensive filtration.

3.6 Adsorption mechanism

The adsorbent material was characterized using SEM and TEM to gain a clearer understanding of the micro-morphological changes in MAC following the adsorption of OTC. TEM (Figures 2a, b) and SEM images (Figures 7a, b) indicated that the morphology of MAC remained largely unchanged after adsorption; however, some OTC moleculars were found to occupy the edges of MAC, resulting in a blurred outline and a roughened surface (Figures 2a, b). The pores of the MAC were filled with OTC, leading to a reduction in surface area (Figures 3b, c). The FT-IR spectrum (Figure 3a) revealed a shift in the absorption peak at 3379 cm^{-1} after adsorption, likely due to the formation of hydrogen bonds between the benzene ring in the OTC molecular structure and corresponding functional groups in the MAC (Miao et al., 2021). Furthermore, XRD analysis (Figure 3e) showed a partial alteration in the crystal structure after adsorption, indicating the occurrence of specific chemical processes, which aligned with the FT-IR findings. Notably, the peak shape in the XRD images exhibited significant changes with in the 0-20° range, potentially indicating anion and cation exchange facilitated by certain electrostatic interactions.

The results of XPS peaks analysis after adsorption indicated that the positions of the two Fe 2p peaks shifted to some extent (Figure 7c). Additionally, the intensity of Fe-O peak decreased, while the Fe 2p peak exhibited a notable intensity corresponding to Fe_2O_3. The C1s spectrum was deconvoluted into three peaks (Figure 7d), representing C-C (284.7 eV, 48.9%), C-O (285.9 eV,

19.4%), and C=O (288.6 eV, 31.7%). The high-resolution O1s spectrum displayed four peaks (Figure 7e), corresponding to Fe-O (530.2 eV), C=O (531.6 eV), O-H (533.6 eV), and O-C (534.0 eV) (Wu et al., 2023). Following adsorption, OTC molecules were detected on the surface of the MAC. Furthermore, the primary N peak observed originated from NH_2-C=O (400.3 eV) in OTC (Figure 7f), although its intensity was relatively low.

According to the characterization provided, the kinetic model analysis and adsorption site energy analysis indicated that the adsorption of OTC by MAC is a physical-chemical process. The proposed adsorption mechanism was presented in Figure 8. The well-developed microporous structure of MAC facilitated pore filling, enhancing the diffusion of OTC into and out of the adsorbent surface. Under acidic conditions, the negatively charged MAC was electrostatically attracted to the positively charged protonated amino group and other functional groups of OTC. Conversely, as pH increased, mutual repulsion became more pronounced, leading to a decrease in adsorption. The functional groups on the surface of MAC, characterized by FT-IR spectra before and after absorption, played a crucial role in the chemical adsorption process. Additionally, the mutual superposition of π-π EDA interactions between MAC (as a π-electron donor) and the benzene rings of OTC (as π-electron acceptors). Additionally, the electron cloud of magnetic particles enhances the π-π stacking interaction between the carbon matrix and antibiotics. The formation of H-bonds on the activated carbon may further enhance adsorption.

4 Conclusions

A MAC with high adsorption efficiency was synthesized using the alkaline co-precipitation method, resulting in a large specific surface area of 555 m^2/g, a stable structure, and abundant nano-pores (4.79 nm), along with various functional groups. The equilibrium adsorption and removal rate of OTC were significantly greater than those of Fe_3O_4. The adsorption process was notably influenced by pH and temperature. Faster equilibrium was achieved, with PFO model providing the best fit on adsorption kinetics in both MAC and Fe_3O_4 systems. The data confirmed to the Langmuir adsorption model, with maximum adsorption capacities of MAC for OTC at temperatures of 20, 25, 30, 35, and 40°C being 93, 112, 118.5, 108 and 117 mg/g, respectively. Both chemisorption and physisorption mechanisms were involved in the OTC removal process, with the adsorption site energy range determined to be between 4 and 16 kJ/mol. However, chemical adsorption was likely the predominant mechanism, facilitated by π-π EDA interactions and H-bonds. The findings highlight the strong adsorptive reactivity of MAC towards OTC and its broad environmental adaptability, which might be well-suited for remediating natural and engineered aquatic systems contaminated by OTC. Further research should consider the effects of other ion and the regeneration and reusability of carbon nanomaterials, as well as the factorial experimental design to find out the optimum variable conditions for OTC adsorption.

Data availability statement

The original contributions presented in the study are included in the article/supplementary material, further inquiries can be directed to yrpi@outlook.com.

Author contributions

WJ: Data curation, Investigation, Methodology, Writing – original draft. LS: Writing – review & editing. HL: Writing – review & editing. TL: Investigation, Writing – review & editing. YT: Writing – review & editing. YP: Conceptualization, Funding acquisition, Supervision, Writing – review & editing.

Funding

The author(s) declare financial support was received for the research and/or publication of this article. This research was financially supported by the Shandong Provincial Natural Science Foundation Grant number: ZR2022QD018(); Yantai University Doctoral Start-up Foundation Grant number: HX2018B32(). This research was also supported by the visiting research fund for teachers of ordinary undergraduate universities in Shandong Province.

Conflict of interest

The authors declare that the research was conducted in the absence of any commercial or financial relationships that could be construed as a potential conflict of interest.

Generative AI statement

The author(s) declare that no Generative AI was used in the creation of this manuscript.

Any alternative text (alt text) provided alongside figures in this article has been generated by Frontiers with the support of artificial intelligence and reasonable efforts have been made to ensure accuracy, including review by the authors wherever possible. If you identify any issues, please contact us.

Publisher's note

References

Altaf, S., Zafar, R., Zaman, W. Q., Ahmad, S., Yaqoob, K., Syed, A., et al. (2021). Removal of levofloxacin from aqueous solution by green synthesized magnetite (Fe_3O_4) nanoparticles using *Moringa olifera*: Kinetics and reaction mechanism analysis. *Eotox. Environ. Safe.* 226, 112826. doi: 10.1016/j.ecoenv.2021.112826

Andrade, C. A., Zambrano-Intriago, L. A., Oliveira, N. S., Vieira, J. S., Quiroz-Fernández, L. S., and Rodríguez-Díaz, J. M. (2020). Adsorption behavior and mechanism of oxytetracycline on rice husk ash: Kinetics, equilibrium, and thermodynamics of the process. *Water Air Soil pollut.* 231, 103. doi: 10.1007/s11270-020-04473-6

Aravind, M., Amalanathan, M., Mary, M. S. M., Parvathiraja, C., Alothman, A. A., Wabaidur, S. M., et al. (2022). Enhanced photocatalytic and biological observations of green synthesized activated carbon, activated carbon doped silver and activated carbon/silver/titanium dioxide nanocomposites. *J. Inorg. Organomet.* P. 32, 267–279. doi: 10.1007/s10904-021-02096-w

Badmus, K. O., Tijani, J., Massima, E., and Petrik, L. (2018). Treatment of persistent organic pollutants in wastewater using hydrodynamic cavitation in synergy with advanced oxidation process. *Environ. Sci. Pollut. R.* 25, 7299–7314. doi: 10.1007/s11356-017-1171-z

Baghdadi, M., Ghaffari, E., and Aminzadeh, B. (2016). Removal of carbamazepine from municipal wastewater effluent using optimally synthesized magnetic activated carbon: adsorption and sedimentation kinetic studies. *J. Environ. Chem. Eng.* 4, 3309–3321. doi: 10.1016/j.jece.2016.06.034

Balzer, F., Zuehlke, S., and Hannappel, S. (2016). Antibiotics in groundwater under locations with high livestock density in Germany. *Water Sci. Tech-W* Sup. 16, 1361–1369. doi: 10.2166/ws.2016.050

Baskan, G., Açıkel, Ü., and Levent, M. (2022). Investigation of adsorption properties of oxytetracycline hydrochloride on magnetic zeolite/Fe_3O_4 particles. *Adv. Powder Technol.* 33, 103600. doi: 10.1016/j.apt.2022.103600

Bednárek, J., Matejová, L., Koutník, I., Vráblová, M., Cruz, G. J. F., Strasák, T., et al. (2024). Revelation of high-adsorption-performance activated carbon for removal of fluoroquinolone antibiotics from water. *Biomass Conversion Bio.* 14, 2585–2599. doi: 10.1007/s13399-022-02577-z

Carter, L. J., Harris, E., Williams, M., Ryan, J. J., Kookana, R. S., and Boxall, A. B. A. (2014). Fate and uptake of pharmaceuticals in soil-plant systems. *J. Agric. Food Chem.* 62, 816–825. doi: 10.1021/jf404282y

Carter, M. C., Kilduff, J. E., and Weber, W. J. (1995). Site energy distribution analysis of preloaded adsorbents. *Environ. Sci. Technol.* 29, 1773–1780. doi: 10.1021/es00007a013

Cevallos-Mendoza, J. E., Cedeño-Muñoz, J. S., Navia-Mendoza, J. M., Figueira, F., Amorim, C. G., Rodríguez-Díaz, J. M., et al. (2024). Development of hybrid MIL-53(Al)@CBS for ternary adsorption of tetracyclines antibiotics in water: Physical interpretation of the adsorption mechanism. *Bioresour. Technol.* 396, 130453. doi: 10.1016/j.biortech.2024.130453

Cheng, X. C., Duan, C. Y., Yang, P., Pi, Y. R., Qi, H. L., Sun, Z. K., et al. (2023). Effective adsorption of crystal violet onto magnetic nanoparticles decorated bacteria: Kinetic and site energy distribution analysis. *Process Saf. Environ.* 173, 837–846. doi: 10.1016/j.psep.2023.03.035

Duan, M. L., Li, H. C., Gu, J., Tuo, X. X., Sun, W., Qian, X., et al. (2017). Effects of biochar on reducing the abundance of oxytetracycline, antibiotic resistance genes, and human pathogenic bacteria in soil and lettuce. *Environ. pollut.* 224, 787–795. doi: 10.1016/j.envpol.2017.01.021

Duan, S., Gao, Y., Lan, G., Qiu, H., Xu, B., Liu, X., et al. (2024). Construction of ligand functionalized MIL-101(Fe)-R and mechanism of efficient removal of chlortetracycline hydrochloride: Experiment and DFT calculation. *Sep. Purif. Technol.* 348, 127753. doi: 10.1016/j.seppur.2024.127753

Fang, N., He, Q., Sheng, L., Xi, Y., Zhang, L., Liu, H., et al. (2021b). Toward broader applications of iron ore waste in pollution control: Adsorption of norfloxacin. *J. Hazard. Mater.* 418, 126273. doi: 10.1016/j.jhazmat.2021.126273

Fang, L., Miao, Y., Wei, D., Zhang, Y., and Zhou, Y. (2021a). Efficient removal of norfloxacin in water using magnetic molecularly imprinted polymer. *Chemosphere* 262, 128032. doi: 10.1016/j.chemosphere.2020.128032

Fatehi, M. H., Shayegan, J., Zabihi, M., and Goodarznia, I. (2017). Functionalized magnetic nanoparticles supported on activated carbon for adsorption of Pb(II) and Cr (VI) ions from saline solutions. *J. Environ. Chem. Eng.* 5, 1754–1762. doi: 10.1016/j.jece.2017.03.006

Foroutan, R., Peighambardoust, S. J., Peighambardoust, S. H., Pareiro, M., and Lorenzo, J. M. (2021). Adsorption of crystal violet dye using activated carbon of lemon wood and activated carbon/Fe_3O_4 magnetic manocomposite from aqueous solutions: A kinetic, equilibrium and thermodynamic study. *Molecules* 26, 2241. doi: 10.3390/molecules26082241

Freundlich, H. M. F. (1906). Over the adsorption in solution. *J. Phys. Chem.* 57, 1100–1107. doi: 10.1515/zpch-1907-5723

Gu, W., Huang, X., Tian, Y., Cao, M., Zhou, L., Zhou, Y., et al. (2021). Appl. *Surf. Sci.* 538, 147813. doi: 10.1016/j.apsusc.2020.147813

He, T., Pan, X., Zhou, W., Ding, H., Liu, M., Xiang, M., et al. (2023). Construction of high-content α-iron on zero-valent iron@biochar composite for the ultra-efficient removal of oxytetracycline hydrochloride: A key step of ammonium bicarbonate pretreatment. *Sep. Purif. Technol.* 323, 124378. doi: 10.1016/j.seppur.2023.124378

Hesas, R. H., Daud, W. M. A. W., Sahu, J. N., and Arami-Niya, A. (2013). The effects of a microwave heating method on the production of activated carbon from agricultural waste: A review. *J. Anal. Appl. Pyrol.* 100, 1–11. doi: 10.1016/j.jaap.2012.12.019

Ho, Y. S., and McKay, G. (1999). Pseudo-second order model for sorption processes. *Process Biochem.* 34, 451–465. doi: 10.1016/S0032-9592(98)00112-5

Homem, V., and Santos, L. (2011). Degradation and removal methods of antibiotics from aqueous matrices - A review. *J. Environ. Mange.* 92, 2304–2347. doi: 10.1016/j.jenvman.2011.05.023

Hu, Q. L., Pang, S. Y., and Wang, D. (2022). In-depth insights into mathematical characteristics, selection criteria and common mistakes of adsorption kinetic kodels: A critical review. *Sep. Purif. Rev.* 51 (3), 281–299.

Jiao, Y., Yi, Y., Fang, Z., and Tsang, P. E. (2024). Selective removal of oxytetracycline by molecularly imprinted magnetic biochar. *Bioresource Technol.* 395, 130394. doi: 10.1016/j.biortech.2024.130394

Kolar, B., Arnus, L., Jeretin, B., Gutmaher, A., Drobne, D., and Durjava, M. K. (2014). The toxic effect of oxytetracycline and trimethoprim in the aquatic environment. *Chemosphere* 115, 75–80. doi: 10.1016/j.chemosphere.2014.02.049

Lagergren, S. K. (1898). About the theory of so-called adsorption of soluble substances. *Sven Vetenskapsakad Handingarl* 24, 1–39.

Langmuir, I. (1916). The constitution and fundamental properties of solids and liquids. Part I. *Solids. J. Am. Chem. Soc* 38, 2221–2295. doi: 10.1021/ja02268a002

Li, X., Gan, T., Zhang, J., Shi, Z., Liu, Z., and Xiao, Z. (2022). High-capacity removal of oxytetracycline hydrochloride from wastewater via Mikania micrantha Kunth-derived biochar modified by Zn/Fe-layered double hydroxide. *Bioresour. Technol.* 361, 127646. doi: 10.1016/j.biortech.2022.127646

Li, R., Zhang, Y., Deng, H., Zhang, Z., Wang, J., Shaheen, S. M., et al. (2020). Removing tetracycline and Hg (II) with ball-milled magnetic nanobiochar and its potential on polluted irrigation water reclamation. *J. Hazard. Mater.* 384, 121095. doi: 10.1016/j.jhazmat.2019.121095

Li, J., Zhang, K. N., and Zhang, H. (2018). Adsorption of antibiotics on microplastics. *Environ. pollut.* 237, 460–467. doi: 10.1016/j.envpol.2018.02.050

Lian, F., Song, Z. G., Liu, Z. Q., Zhu, L. Y., and Xing, B. S. (2013). Mechanistic understanding of tetracycline sorption on waste tire powder and its chars as affected by Cu^{2+} and pH. *Environ. pollut.* 178, 264–270. doi: 10.1016/j.envpol.2013.03.014

Liang, G., Wang, Z., Yang, X., Qin, T., Xie, X., Zhao, J., et al. (2019). Efficient removal of oxytetracycline from aqueous solution using magnetic montmorillonite-biochar composite prepared by one step pyrolysis. *Sci. Total Environ.* 695, 133800. doi: 10.1016/j.scitotenv.2019.133800

Lin, H., Qiu, S., Wu, Z., Ye, X., and Liu, M. (2022). Fabrication of lignin-based biochar containing multi-metal ferrite and efficient removal for oxytetracycline hydrochloride. *J. Clean. Prod.* 331, 129885. doi: 10.1016/j.jclepro.2021.129885

Liu, D., Gu, W., Zhou, L., Lei, J., Wang, L., Zhang, J., et al. (2023). From biochar to functions: Lignin induced formation of Fe_3C in carbon/Fe composites for efficient adsorption of tetracycline from wastewater. *Sep. Purif. Technol.* 304, 122217. doi: 10.1016/j.seppur.2022.122217

Lu, Z. Y., Ma, Y. L., Zhang, J. T., Fan, N. S., Huang, B. C., and Jin, R. C. (2020). A critical review of antibiotic removal strategies: Performance and mechanisms. *J. Water Process Eng.* 38, 101681. doi: 10.1016/j.jwpe.2020.101681

Lv, X., Yan, D. Y. S., Lam, F. L., Ng, Y. H., Yin, S., and An, A. K. (2020). Solvothermal synthesis of copper-doped BiOBr microflowers with enhanced adsorption and visible-light driven photocatalytic degradation of norfloxacin. *Chem. Eng. J.* 401, 126012. doi: 10.1016/j.cej.2020.126012

Lye, J. W. P., Saman, N., Sharuddin, S. S. N., Othman, N. S., Mohtar, S. S., Md Noor, A. M., et al. (2017). Removal performance of tetracycline and oxytetracycline from aqueous solution via natural zeolites: An equilibrium and kinetic study. *Clean-Soil Air Wayer* 45, 1600260. doi: 10.1002/clen.201600260

Ma, Y., Wang, R., Gao, C., and Han, R. (2023). Carbon nanotube-loaded copper-nickel ferrite activated persulfate system for adsorption and degradation of oxytetracycline hydrochloride. *J. Colloid Interf. Sci.* 640, 761–774. doi: 10.1016/j.jcis.2023.03.001

Miao, J., Zhao, X., Zhang, Y., and Liu, Z. (2021). Feasible synthesis of hierarchical porous MgAl-borate LDHs functionalized Fe_3O_4@SiO_2 magnetic microspheres with excellent adsorption performance toward congo red and Cr(VI) pollutants. *J. Alloy. Compd.* 861, 157974. doi: 10.1016/j.jallcom.2020.157974

Mihciokur, H., and Oguz, M. (2016). Removal of oxytetracycline and determining its biosorption properties on aerobic granular sludge. *Environ. Toxicol. Phar.* 46, 174–182. doi: 10.1016/j.etap.2016.07.017

Nasrollahi, N., Vatanpour, V., and Khataee, A. (2022). Removal of antibiotics from wastewaters by membrane technology: Limitations, successes, and future improvements. *Sci. Total Environ.* 838, 156010. doi: 10.1016/j.scitotenv.2022.156010

Pi, Y., Duan, C., Zhou, Y., Sun, S., Yin, Z., Zhang, H., et al. (2022). The effective removal of Congo Red using a bio-nanocluster: Fe_3O_4 nanoclusters modified bacteria. *J. Hazard. Mater.* 424, 127577. doi: 10.1016/j.jhazmat.2021.127577

Ritchie, A. G. (1977). Alternative to the Elovich equation for the kinetics of adsorption of gases on solids. *J. Chem. Soc Faraday Trans. 1 Phys. Chem. Condens Phases* 73, 1650–1653. doi: 10.1039/F19777301650

Saglam, S., Turk, F. N., and Arslanoglu, H. (2024). Synthesis of magnetic activated carbon from industrial waste: characterization, tetracycline removal and interpretation of its mechanism. *Biomass Convers. Bior.* 14, 10791–10805. doi: 10.1007/s13399-023-05229-y

Shao, L., Ren, Z., Zhang, G., and Chen, L. (2012). Facile synthesis, characterization of a $MnFe_2O_4$/activated carbon magnetic composite and its effectiveness in tetracycline removal. *Mater. Chem. Phys.* 135, 16–24. doi: 10.1016/j.matchemphys.2012.03.035

Smata, A., and Yoshimura, C. (2022). One-step synthesis of magnetic-layered double hydroxide and its application for oxytetracycline removal from water. *J. Environ. Chem. Eng.* 10, 107819. doi: 10.1016/j.jece.2022.107819

Song, J., Messele, S. A., Meng, L., Huang, Z., and El-Din, M. G. (2021). Adsorption of metals from oil sands process water (OSPW) under natural pH by sludge-based biochar/chitosan composite. *Water Res.* 194, 116930. doi: 10.1016/j.watres.2021.116930

Sun, M., Yang, Y., Huang, M., Fu, S., Hao, Y., Hu, S., et al. (2022). Adsorption behaviors and mechanisms of antibiotic norfloxacin on degradable and nondegradable microplastics. *Sci. Total Environ.* 807, 151042. doi: 10.1016/j.scitotenv.2021.151042

Tang, Y., Jia, W., Bao, M., Qiu, S., Pi, Y., Liu, C., et al. (2023). Pick-up of fluoroquinolones from the aqueous phase via magnetically propeled microrobots: kinetics, thermodynamics, and site energy distribution analysis. *Front. Mar. Sci.* 10, 1169883. doi: 10.3389/fmars.2023.1169883

Temkin, M. J., and Pyzhev, V. (1940). Recent modifcations to langmuir isotherms. *Acta Physiochim URSS* 12, 217–225.

Wang, S., Ma, X. X., Liu, Y. L., Yi, X. S., Du, G. C., and Li, J. (2020). Fate of antibiotics, antibiotic-resistant bacteria, and cell-free antibiotic-resistant genes in full-scale membrane bioreactor wastewater treatment plants. *Bioresource Technol.* 302, 122825. doi: 10.1016/j.biortech.2020.122825

Wang, X., Yin, R., Zeng, L., and Zhu, M. S. (2019). A review of graphene-based nanomaterials for removal of antibiotics from aqueous environments. *Environ. pollut.* 253, 100–110. doi: 10.1016/j.envpol.2019.06.067

Wang, Z., Yu, X., Pan, B., and Xing, B. (2010). Norfloxacin sorption and its thermodynamics on surface-modified carbon nanotubes. *Environ. Sci. Technol.* 44, 978–984. doi: 10.1021/es902775u

Wu, X. L., Xiang, L., Yan, Q. Y., Jiang, Y. N., Li, Y. W., Huang, X. P., et al. (2014). Distribution and risk assessment of quinolone antibiotics in the soils from organic vegetable farms of a subtropical city, Southern China. *Sci. Total Environ.* 487, 399–406. doi: 10.1016/j.scitotenv.2014.04.015

Wu, Z., Zhang, H., Ali, E., Shahab, A., Huang, H., Ullah, H., et al. (2023). Synthesis of novel magnetic activated carbon for effective Cr(VI) removal via synergistic adsorption and chemical reduction. *Environ. Technol. Inno.* 30, 103092. doi: 10.1016/j.eti.2023.103092

Xiang, W., Zhang, X., Luo, J., Li, Y., Guo, T., and Gao, B. (2022). Performance of lignin impregnated biochar on tetracycline hydrochloride adsorption: governing factors and mechanisms. *Environ. Res.* 215, 114339. doi: 10.1016/j.envres.2022.114339

Xu, X. R., and Li, X. Y. (2010). Sorption and desorption of antibiotic tetracycline on marine sediments. *Chemosphere* 78, 430–436. doi: 10.1016/j.chemosphere.2009.10.045

Yan, L., Liu, Y., Zhang, Y., Liu, S., Wang, C., Chen, W., et al. (2020). $ZnCl_2$ modified biochar derived from aerobic granular sludge for developed microporosity and enhanced adsorption to tetracycline. *Bioresour. Technol.* 297, 122381. doi: 10.1016/j.biortech.2019.122381

Yan, B., Niu, C. H., and Wang, J. (2017). Kinetics, electron-donor-acceptor interactions, and site energy distribution analyses of norfloxacin adsorption on pretreated barley straw. *Chem. Eng. J.* 330, 1211–1221. doi: 10.1016/j.cej.2017.08.056

Yang, N., Zhu, S., Zhang, D., and Xu, S. (2008). Synthesis and properties of magnetic Fe_3O_4-activated carbon nanocomposite particles for dye removal. *Mater. Lett.* 62, 645–647. doi: 10.1016/j.matlet.2007.06.049

Zeng, Q., Chen, K., Huang, X., Luo, S., Wang, X., Luo, D., et al. (2024). Competitive adsorption of oxytetracycline and sulfamethoxazole bynanosized activated carbon in aquatic environments: Experimental analysis and DFT calculations. *Chem. Eng. J.* 499, 156375. doi: 10.1016/j.cej.2024.156375

Zhang, X. Y., Chu, Y. Y., Zhang, H. Y., Hu, J., Wu, F., Wu, X. Y., et al. (2021). A mechanistic study on removal efficiency of four antibiotics by animal and plant origin precursors -derived biochars. *Sci. Total Environ.* 772, 145468. doi: 10.1016/j.scitotenv.2021.145468

Zhang, Y., Li, A. L., Dai, T. J., Li, F. F., Xie, H., Chen, L. J., et al. (2018). Cell-free DNA: A neglected source for antibiotic resistance genes spreading from WWTPs. *Environ. Sci. Technol.* 52, 248–257. doi: 10.1021/acs.est.7b04283

Zhang, F. F., Wang, J., Tian, Y., Liu, C., Zhang, S., Cao, L., et al. (2023a). Effective removal of tetracycline antibiotics from water by magnetic functionalized biochar derived from rice waste. *Environ. pollut.* 330, 121681. doi: 10.1016/j.envpol.2023.121681

Zhang, X., Zhen, D., Liu, F., Chen, R., Peng, Q., and Wang, Z. (2023b). An achieved strategy for magnetic biochar for removal of tetracyclines and fluoroquinolones: adsorption and mechanism studies. *Bioresour. Technol.* 369, 128440. doi: 10.1016/j.biortech.2022.128440

Zhao, H., Liu, X., Cao, Z., Zhan, Y., Shi, X. D., Yang, Y., et al. (2016). Adsorption behavior and mechanism of chloramphenicols, sulfonamides, and non-antibiotic pharmaceuticals on multi-walled carbon nanotubes. *J. Hazard. Mater.* 310, 235–245. doi: 10.1016/j.jhazmat.2016.02.045

Zhou, Y., Luan, L., Tang, B., Niu, Y., Qu, R., Liu, Y., et al. (2020). Fabrication of Schiff base decorated PAMAM dendrimer/magnetic Fe_3O_4 for selective removal of aqueous Hg(II). *Chem. Eng. J.* 398, 125651. doi: 10.1016/j.cej.2020.125651

Zhou, Q., Wang, Y., Xiao, J., Fan, H., and Chen, C. (2019). Preparation and characterization of magnetic nanomaterial and its application for removal of polycyclic aromatic hydrocarbons. *J. Hazard. Mater.* 371, 323–331. doi: 10.1016/j.jhazmat.2019.03.027